Field-induced diverse quantizations in monolayer and bilayer black phosphorus

Jhao-Ying Wu,[1,*] Szu-Chao Chen,[2,†] Godfrey Gumbs,[3,‡] and Ming-Fa Lin[2,§]

[1]*Center of General Studies, National Kaohsiung Marine University, Kaohsiung, Taiwan 811*
[2]*Department of Physics, National Cheng Kung University, Tainan, Taiwan 701*
[3]*Department of Physics and Astronomy, Hunter College at the City University of New York, 695 Park Avenue,*
New York, New York 10065, USA

This report provides a comprehensive understanding of the magnetic quantization effects in phosphorene with the use of the generalized tight-binding model. Especially for bilayer systems, a composite magnetic and electric field can induce the feature-rich LL spectrum. We demonstrate the existence of two subgroups of Landau levels (LLs) near the Fermi level according to their distinguishable localization centers. The strong competition between the two subgroups induces unusual quantization behaviors, such as multiple anticrossings for the B_z- and E_z-dependent energy spectra. These results are clearly explained by the spatial distributions of subenvelope functions from which two types of LLs are characterized by being either the usual or the perturbed distribution modes. The detailed analysis of the diverse magnetic quantizations is quite important in understanding other physical properties, such as the dispersion relations of magnetoplasmons, magneto-optical selection rules, as well as electron transport properties. The unusual energy spectra are directly revealed by the special features of the density of states, which could be further validated by measurements employing scanning tunneling spectroscopy.

I. INTRODUCTION

Two-dimensional (2D) layered systems, with nanoscale thickness and unique geometric symmetries, have initiated considerable experimental and theoretical studies [1–3]. They have been successfully synthesized by various experimental methods to produce for example graphene [4], silicene [5], germanene [6], tinene [7], and transition metal oxides [8]. Such 2D systems are very suitable for studying novel physical, chemical, and material phenomena. Specifically, few-layer black phosphorus (phosphorene) has been produced recently by using mechanical cleavage [9,10], liquid exfoliation [11–13], and the mineralizer-assisted short-way transport reaction [14–16]. These structures inherently have energy band gaps of $\sim 0.5-2$ eV [17–19], as identified from optical measurements [10,20]. Such gaps are higher than that (~ 0.3 eV) for the bulk [9,17,21], and are in sharp contrast with the zero or narrow gaps of 2D group-IV materials [22]. Transport measurements show that a phosphorene-based field-effect transistor exhibits an on/off ratio of 10^5 and a carrier mobility at room temperature as high as 10^3 cm^2/V s [9]. Additionally, the layered black phosphorus systems display unusual energy spectra and quantum Hall effects due to magnetic quantization [23–28]. Similar calculations have been performed on phosphorene ribbons [25,27]. In a ribbon geometry, the competition between the quantum confinement and magnetic quantization would lead to partially dispersionless energy spectra [29]. Few-layer black phosphorus is expected to have unparalleled potential in the next-generation electronic and optical devices [9,30]. Our work is focused on how to produce diverse quantization phenomena in monolayer and bilayer black phosphorus by tuning a composite magnetic and electric field ($\mathbf{B} = B_z\hat{z}$ and $\mathbf{E} = E_z\hat{z}$).

Each phosphorene layer possesses a puckered structure, mainly due to the sp^3 hybridization of $(3s,3p_x,3p_y,3p_z)$ orbitals. The deformed hexagonal lattice in the x-y plane is quite different from the honeycomb lattice of group-IV systems [18]. This unique geometric structure fully dominates the low-lying energy bands which are highly anisotropic in the energy dispersion relations versus the wave vector, e.g., the linear and parabolic dispersions near the Fermi energy E_F, respectively, along the $\widehat{k_x}$ and $\widehat{k_y}$ directions [18]. The anisotropic behaviors are clearly revealed in other physical properties, as verified by recent measurements of the optical spectra and transport properties [9,30]. This provides a unique advantage for phosphorene in comparison with MoS$_2$ and related semiconductors. The unusual anisotropy could be utilized in the design of unconventional thermoelectric devices. For example, the thermal gradient and potential difference could be applied in two orthogonal directions, leading to one having higher thermal conductivity and another with larger electrical conductivity [31]. Moreover, this intrinsic property will greatly diversify the quantization phenomena.

The low-lying electronic band structure is easily tuned by an external electric and magnetic field. A uniform perpendicular electric field can create a monotonic increase in the energy band gap for monolayer phosphorene. In contrast, a high-frequency laser field could close the band gap [32]. For bilayer black phosphorus there are drastic changes in the energy bands producing a gapless band structure after reaching a critical electric field ($E_{z,c}$) [33,34]. There exist rich energy dispersions as E_z is varied, including the appearance of parabolic bands, graphene-like Dirac cones, and oscillatory energy bands. These unusual transitions arise from a strong competitive or cooperative relation between the intralayer and interlayer atomic interactions and the Coulomb potentials.

―――――――

*yarst5@gmail.com
†szuchaochen@gmail.com
‡ggumbs@hunter.cuny.edu
§mflin@mail.ncku.edu.tw

These will be directly exhibited in the diverse magnetic quantization phenomena. The generalized tight-binding (TB) model is further developed to explore the essential electronic properties in detail [35]. The Hamiltonian is built from the TB functions on distinct sublattices and layers for which all interactions and external fields are taken into account simultaneously. This method can deal with the the magnetic quantization of electronic states even in the presence of complicated geometrical structures and external fields [35,36]. Our procedure gives the correct Landau level (LL) spectrum and wave functions out of the magnetically enlarged unit cell (see Sec. II). This is essential for obtaining reliable physical properties, such as magneto-optical and Coulomb excitations. We report on the application of this numerically intensive procedure to black phosphorus.

The dispersionless LLs come from the magnetic quantization of neighboring electronic states. The main features are investigated for monolayer and bilayer black phosphorus in the presence of a combined electric and magnetic field, especially for the B_z- and E_z-dependent energy spectra and the spatial distributions of quantum modes. The generalized TB model is suitable for investigating the competitive quantization due to the multiconstant energy loops and the coexistent extreme and saddle points in the energy-wave-vector space. This study shows that the LL spectra exhibit a monotonic or nonmonotonic dependence, and noncrossing, crossing, or anticrossing behaviors. Furthermore, we obtain two types of LLs characterized by being either the usual or the perturbed distribution modes. The anticrossing spectra will be clearly illustrated by obvious changes in the mixed modes. Specifically, two distinct subgroups of valence (conduction) LLs near the Fermi level are identified from the distinguishable localization centers. . The energy spectra are directly revealed in the special structures of density of states (DOS). They could be verified from experimental measurements of scanning tunneling spectroscopy (STS).

II. METHODS

Monolayer phosphorene, with a puckered honeycomb structure, has a primitive unit cell containing four phosphorus atoms, as plotted by the dashed green lines in Fig. 1(a). Two of the four phosphorus atoms are located on the lower (red circles) or higher (blue circles) sublattice sites. Similar structures are revealed in few-layer systems, e.g., bilayer phosphorene as shown in Fig. 1(b). The low-lying energy bands are dominated by the atomic interactions of $3p_z$ orbitals [18]. The few-layer Hamiltonian is characterized by

$$H = \sum_{i=1,l}^{4} \left(\varepsilon_i^l + U_i^l \right) c_i^l c_i^{\dagger l} + \sum_{\langle i,j \rangle, l} t_{ij}^{ll} c_i^l c_j^{\dagger l} + \sum_{\langle i,j \rangle, l \neq l'} t_{ij}'^{ll'} c_i^l c_j^{\dagger l'}.$$

(1)

Here, ε_i^l is zero in a monolayer; for a few-layer system, it is a layer- and sublattice-dependent site energy due to the chemical environment. Also, U_i^l is the Coulomb potential energy induced by an electric field. They both contribute to the diagonal matrix elements. In the absence of a magnetic field, the summation is written as $\Sigma_{i=1,l}^{4}$, but in the presence of a magnetic field it becomes $\Sigma_{i=1,l}^{4R_B}$ (seen later). In our notation,
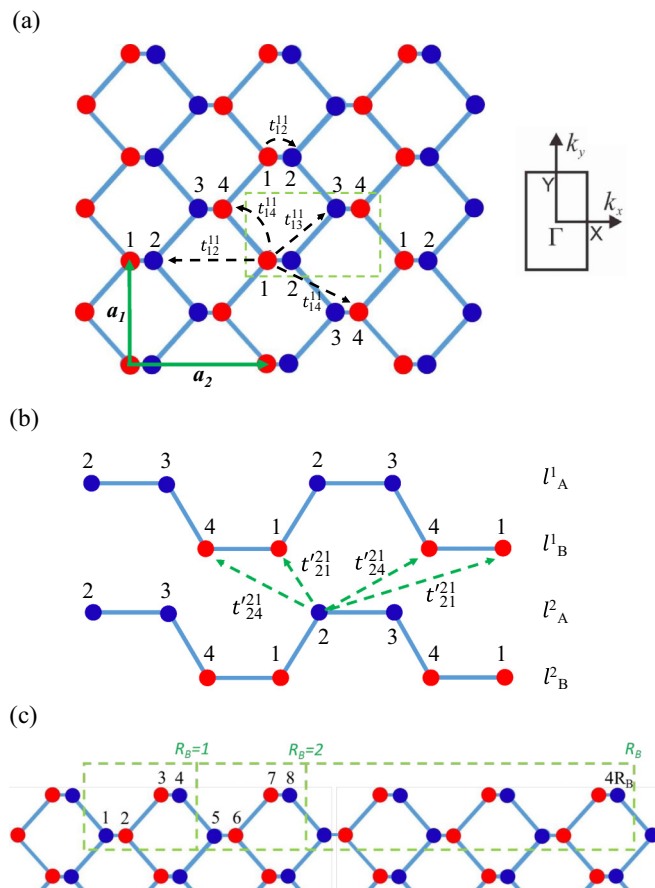
FIG. 1. Geometric structures of (a) monolayer and (b) bilayer phosphorus, respectively, for the top and side views with various atomic interactions. Also shown is the first Brillouin zone. The magnetically enlarged unit cell for monolayer is depicted in (c).

c_i^l ($c_j^{\dagger l'}$) is an annihilation (creation) operator, t_{ij}^{ll} and $t_{ij}'^{ll'}$ are, respectively, the intralayer and interlayer hopping integrals, and the effective interactions used in the calculations cover the fourth and fifth neighboring atoms. These hopping parameters have been adopted from Ref. [18].

Monolayer and bilayer black phosphorus are assumed to be present in an applied uniform perpendicular magnetic field. The magnetic flux through a unit rectangle is $\Phi = a_1 a_2 B_z$, where $a_1 = 3.27$ Å and $a_2 = 4.43$ Å are lattice constants [the lattice vectors are shown by the green arrows in Fig. 1(a)]. The vector potential, $\vec{A} = (B_z x)\hat{y}$, can create an extra magnetic Peierls phase of $\exp\{i[\frac{2\pi}{\phi_0} \int \vec{A} \cdot d\vec{r}]\}$, leading to a new period along $\hat{x}$ and thus an enlarged rectangular unit cell with $4R_B = 4\phi_0/\Phi$ atoms in a monolayer, as illustrated in Fig. 1(c). Here, ϕ_0 ($=h/e = 4.1 \times 10^{-15}$ T m^2) is the magnetic flux quantum; ϕ_0/Φ is chosen to be an integer. The reduced first Brillouin zone has an area of $4\pi^2/a_1 a_2 R_B$. For bilayer black phosphorus, the magnetic Hamiltonian matrix is very large with $8R_B \times 8R_B$ matrix elements within achievable experimental field strengths, e.g., the dimension of 16 800 at $B_z = 30$ T. The calculation procedure for a two-dimensional system is in a large contrast to that for a one-dimensional ribbon [27]. In ribbons, the periodicity along the longitudinal direction (parallel to the edges) can be independent of the

magnetic field in a chosen Landau gauge. The quantum confinement would hinder the magnetic quantization, leading to the partially dispersionless energy spectra [29] rather than the dispersionless LLs in a two-dimensional system.

The generalized tight-binding model is based on the subenvelope functions of the constituent sublattices [35]. The calculation method is quite different from that in Ref. [28]. In the latter, the magneto-electronic states are the linear superposition of original k states in zero fields; that is, the wave functions are the superposition of wave-vector-dependent states rather than the real-space tight-binding functions. The spatial distributions of subenvelope functions derived from the generalized tight-binding model are utilized to characterize the magnetic quantum numbers and the types of LLs. They are useful for explaining the peculiar LL behaviors (discussed later). To achieve the experimentally attainable field strengths, a bandlike matrix is developed to solve the huge matrix efficiently [35]. Accordingly, we observe the strong electrically tunable LL spectra in $B_z < 60$ T. The methodology simultaneously incorporates the intralayer and interlayer atomic interactions and the effects of external fields. It is applicable to study the quantization effect in arbitrarily stacked layered materials under any form of external fields. Moreover, the results are accurate and reliable within a wide energy range.

III. RESULTS AND DISCUSSION

A special lattice structure and multiple hopping integrals are responsible for the rich energy bands of the black phosphorus structures we are investigating here. Monolayer phosphorene has a direct gap of $E_g \sim 1.6$ eV near the Γ point as illustrated in Fig. 2(a), while group-IV systems have zero or narrow gaps at the K point [37]. Along the ΓX and ΓY directions, the energy dispersion relations are approximately linear and parabolic, respectively. The effective mass along ΓX is different than ΓY, being affected by the preferred chemical bonding along $\hat{x}$ [34]. The conduction and valence bands are asymmetric about $E_F = 0$. They, respectively, arise from linearly symmetric and antisymmetric superpositions of TB functions on the two A and B sublattices. This simple relation for the same layer is modified in bilayer black phosphorus, mainly as a result of the finite site energies appearing as the first term in Eq. (1). Furthermore, the smaller band gap of $E_g \sim 1.01$ eV is reduced by the interlayer atomic interactions.

A perpendicular electric field can greatly diversify the electronic properties. The band gap E_g of the monolayer is increased monotonically as the field strength is increased, shown in Figs. 2(a) and 2(b) (E_z is in units of V/Å). For bilayer black phosphorus, the first pair of energy bands approaches E_F [Figs. 2(c)–2(f)], whereas the opposite applies for the second pair. The parabolic bands of the former lead to a zero band gap near the Γ point at the critical field $E_{z,c} \approx 0.3$ as shown in Fig. 2(f). With a further increase in field strength, their energy dispersions have a dramatic change, illustrated in Fig. 2(g). Along ΓY and ΓX (unit vectors $\hat{k}_x$ and $\hat{k}_y$), there exist linearly intersecting bands and oscillatory bands, respectively. Two split Dirac-cone structures are situated on the right- and left-hand sides of the Γ point [along $+\hat{k}_y$ and $-\hat{k}_y$ in Fig. 2(h)]. Furthermore, the extremum points are just

at the Γ point, accompanied with two saddle points on the opposite $k'_x s$. All the critical points and the constant-energy loops in the energy-wave-vector space will dominate the main features of the LL spectra. Specifically, the Coulomb potential energy differences can create significant probability transfer between two layers. For example, four TB functions might be extremely noncomparable for a sufficiently high field strength. This will play a crucial role in the forms of the unusual LL wave functions.

The highly anisotropic energy dispersion relation generates a unique dependence of LL energies on the quantum number $n^{c,v}$, which we discuss below, and the magnetic filed strength, as shown in Fig. 3. Each LL is four-fold degenerate for each (k_x, k_y) state because of the spin degree and the mirror symmetry about the z axis. The $(k_x = 0, k_y = 0)$ state in the reduced Brillouin zone is chosen for a systematic study. In monolayer and bilayer phosphorus, the low-lying LL energies cannot be well described by a linear relation $n^{c,v} B_z$ (the dashed pink lines), especially for the higher energy and field strength. This is different from the square-root dependence in monolayer graphene [38], and the linear dependence in AB-stacked bilayer graphene [39] and MoS$_2$ [40]. There are two groups of valence and conduction LLs in bilayer phosphorus [the right panel of Fig. 3(b)]. Both of them cross each other frequently, for which the main differences lie in the initiated energies and the resulting LL spacings. Specifically, the initial LL energy corresponds to that of the extremum point in the zero-B_z energy band. The intragroup and intergroup anticrossings, as revealed in intrinsic ABC-stacked graphene [35], are absent, since all the well-behaved LLs are quantized from the monotonic band structure in energy-wave-vector space, which we present in Figs. 2(a) and 2(c).

The main features of the LLs are dramatically changed by the electric field for $E_z \geqslant E_{z,c}$. The LL spectrum could be divided into three regimes according to the energy ranges of the distinct energy dispersion, e.g., $E_z = 0.32$ in Figs. 4(a) and 4(b). Regimes (I), (II), and (III), respectively, correspond to the Dirac cone (green), the inner and outer parabolic bands (between the saddle and extremum points; blue and pink curves), and the parabolic curve (below or above the extremum point, i.e., the pink curve). In (I), the zero-energy LLs are formed at the Fermi level, clearly indicating the magnetic quantization is initiated from the E_z-induced Dirac point (the extremum point). Eigenstate degeneracy of the low-lying LLs is twice that for others, mainly due to the two Dirac-cone features shown in Fig. 2(h). The LL energy spacings rapidly decrease with increased quantum number. Specifically, the LLs in regime (II) present an abnormal sequence, since they come from a strong competition between magnetic quantization in the two distinct constant-energy loops. The LL spectrum becomes well behaved in (III), and its energy spacing is almost uniform. This directly reflects the normal monotonic quantization for a parabolic band.

The feature-rich LL spectrum could be fully understood from the Landau wave functions. The subenvelope functions are distributed onto the different sublattices and layers. They are localized near the 1/2 and 2/2 positions of the enlarged unit cell in the crystal lattice space, being related to the magnetic quantization at the Γ point. These states contribute to the initial LL energy spectra. Similar localization behaviors occur
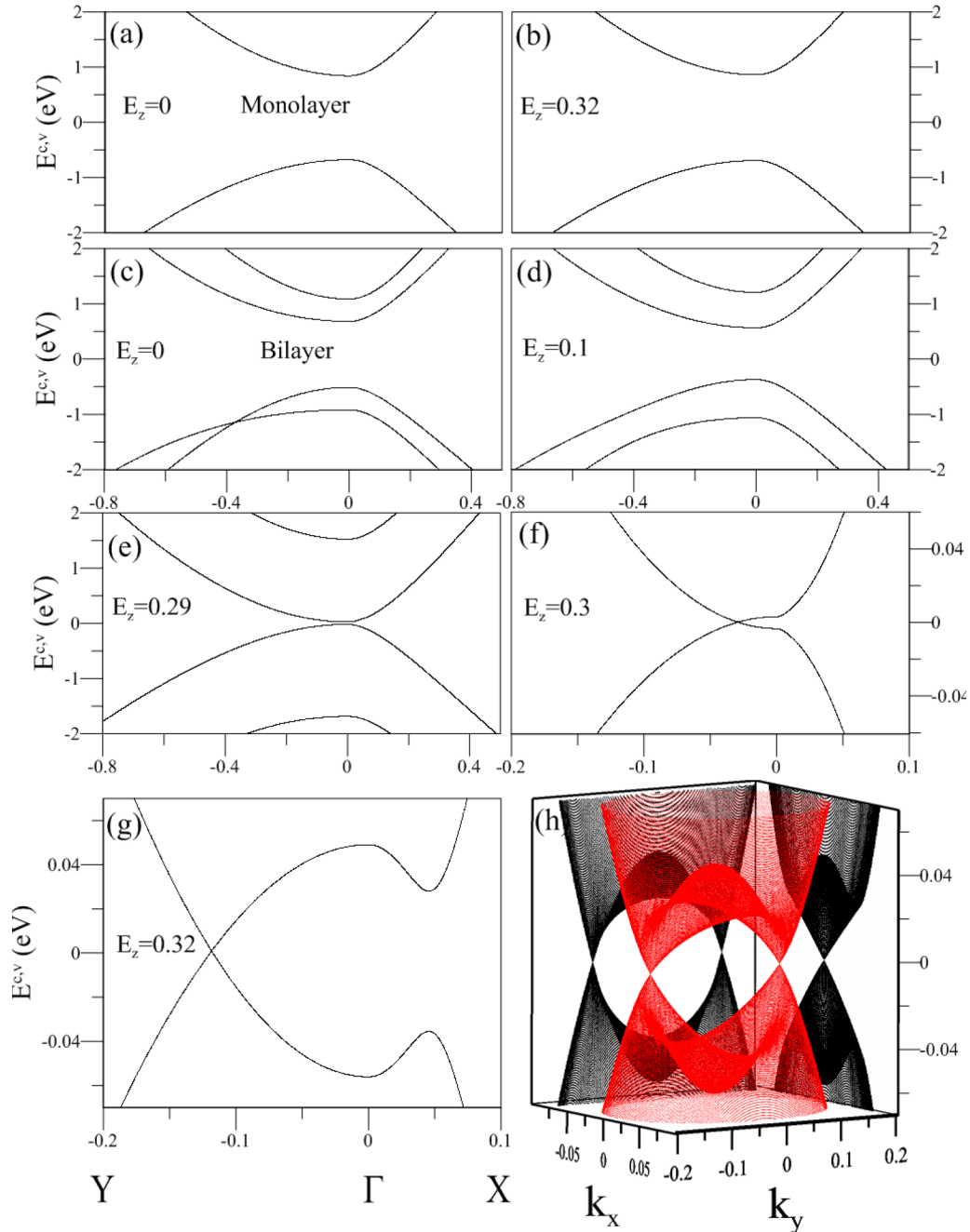
FIG. 2. E_z-induced changes of electronic structures for monolayer phosphorene in (a) and (b) and bilayer system in (c)–(g). At $E_z = 0.32$, the diverse band dispersions in energy-wave-vector space is shown in (h).

around the two centers, so the 1/2 position is sufficient for a model study. In general, the identical oscillation modes are revealed in the two sublattices for the same layer. The number of zero points in the dominant amplitude distribution is the quantum number. There are the coexistent main and side modes for the low-lying LL states at $E_z \geqslant E_{z,c}$, a feature due to the cooperation of the multihopping integrals, the Coulomb potential energies, and the magnetic field. The subenvelope functions in regime (I) are simultaneously localized on the left- and right-hand sides of the 1/2 position as shown in Figs. 4(c) and 4(d), in which the two degenerate states possess the same weight on the two sublattices and layers depicted

by light and heavy green curves. They are associated with the magnetic quantization of two neighboring Dirac cones. Such LL states are regarded as the first subgroup of valence LLs. When state energies are a little away from the Dirac points, the zero points in the spatial oscillations increase. The two separate localization centers then merge, thereby reducing the LL degeneracy fourfold at $E^v < -0.034$ eV. The zero-point numbers of the l_A^1 and l_A^2 components quickly increase (pink curves) when entering into (II). The well-defined oscillation modes of many zero points clearly demonstrate that such LLs come from the quantized states of the larger constant-energy loop. On the other hand, the smaller constant-energy loop can
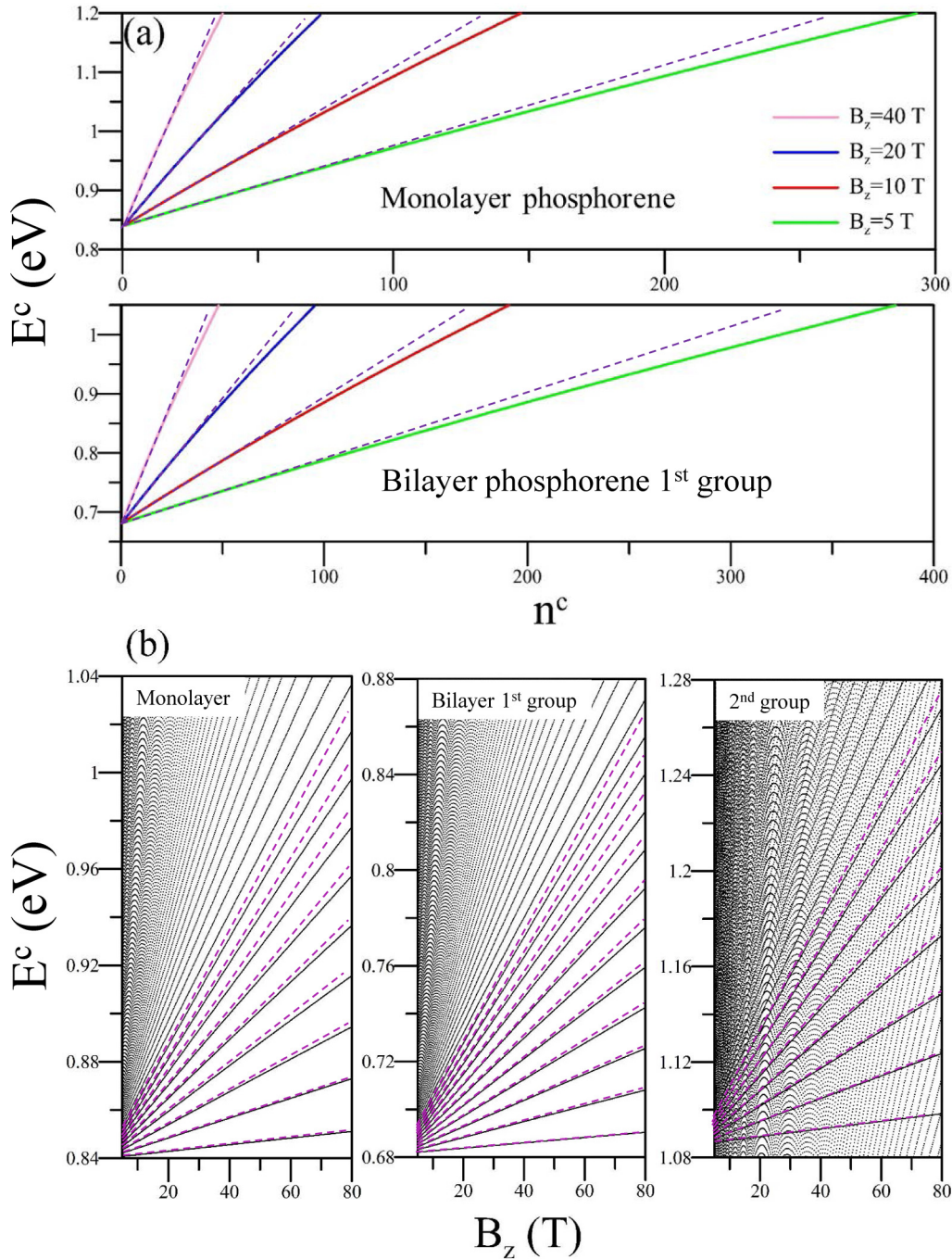
FIG. 3. n^c-dependent LL energy spectra of monolayer and bilayer phosphorus at various B_z, and (b) for the B_z-dependent ones.

create a second subgroup of LLs (blue curves). The initial LLs at -0.053 eV, with the dominant zeroth mode in the l_A^1 component, correspond to magnetic quantization near the Γ point. The competitive quantization between two distinct loops leads to the unfamiliar LL sequence and spatial oscillations in (II). That is, there exist crossings and anticrossings of two subgroups as shown in Fig. 5(a). The subenvelope functions in regimes (I) and (II) do not present a single-mode oscillation, and their components on the two layers differ from each other. But for (III), they are all well-behaved oscillation modes arising from the monotonic parabolic dispersion, i.e., they are identical to those of a quantized simple harmonic oscillator

[39]. Specifically, the LL wave functions exhibit the same oscillation modes on the two separate layers. In short, the two subgroups of LLs are the magnetically quantized states near the Dirac and Γ points. Their strong competition induces the unusual quantization behaviors.

The LL energy spectra, shown in Figs. 5(a) and 5(b), are greatly diversified by applying external fields. The valence and conduction LLs exhibit similar B_z- and E_z-dependent spectra. The former in regime (I) have a well-behaved B_z-dependence when the magnetic field is less than 20 T which can be seen from Fig. 5(a). Their energies could be fitted by a square-root relation $\sqrt{n_D^v B_z}$. This dependence is similar
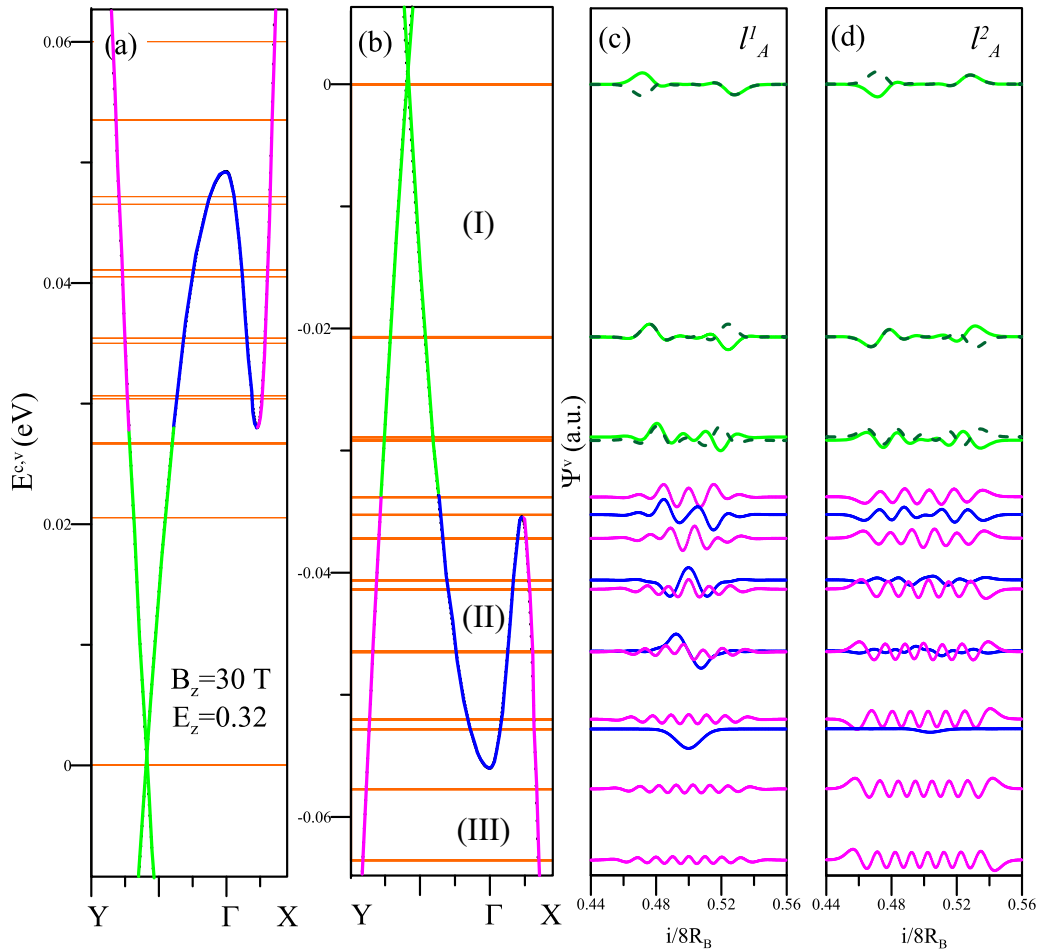
FIG. 4. At $E_z = 0.32$, (a) the conduction and (b) valence LLs, and the subenvelope functions of the latter on the (c) first and (d) second layers. The x axis in (c) and (d) presents the locations of phosphorus atoms in the enlarged unit cell. This unit cell contains a total of $8R_B$ atoms. Moreover, the different colors used for the curves are associated with the two distinct constant-energy loops and the three energy regions in (b).

to that of monolayer graphene with a linear Dirac cone [38]. However, the two entangled LLs, which arise from the anticrossing of two subgroups, appear at higher magnetic fields. As for the valence LLs in (II), their spectrum presents two coexistent subgroups for the nonmonotonic relations. Furthermore, the n_D^v and n_Γ^v LLs have opposite B_z dependence. The crossings and anticrossings occur continuously in an alternative form. This abnormal B_z-dependent spectrum has not been reported in other 2D materials. Thus, the unusual LL spectrum of two competitive subgroups is absent in other layered systems. The anticrossings clearly illustrate that such LLs are composed of multioscillation modes seen in Fig. 6. With the deeper state energies, the LL spectrum changes into the monotonic B_z dependence, directly reflecting the parabolic energy dispersion. All the LLs in regime (III) belong to single-mode oscillations with many zero points. The complicated LL spectra are also achieved by tuning the electric field. At $E_z > E_{z,c}$ for which we refer to Fig. 5(b), there exist frequent crossings and anticrossings related to the two subgroups of LLs. The diverse LL spectra will be obviously revealed in DOSs as special structures, so that they could be directly identified from the STS measurements.

The anticrossing spectra originate from the Landau states with the multiple zero points. That is, the LLs are composed of

multioscillation modes, including a main mode and certain side modes. To prevent the mixed LLs from crossing each other, both of them must have identical oscillation modes. The drastic changes of the wave functions during the anticrossing process between the fourth LLs in the first and second subgroups are illustrated in Figs. 6(a) and 6(b) (blue and pink curves). The anticrossing region occurs in the range ∼27.6−31.5 T, where the most hybridization of the two levels is present at its center. At the initial field strength, both $n_D^v = 3$ and $n_\Gamma^v = 3$ LLs have the main mode of three zero points in the l_A^1 component. Furthermore, the former possesses side modes with five, seven, and nine zero points. The latter presents similar side modes for an increase of B_z. The side modes are enhanced, but the main mode weakened. Such oscillation modes are mixed at the anticrossing center ($B_z = 29.6$ T). And then, the mutlioscillation modes gradually become the typical ones. Similar transformation of oscillation modes are revealed in the l_A^2 component, in which the main and side modes of the two anticrossing LLs, respectively, correspond to 10 and (4,6,8,12) zero points. The frequent LL anticrossings occur in the B_z- and E_z-dependent energy spectra of Figs. 5(a) and 5(b), since the external fields and the intralayer and interlayer atomic interactions strongly compete or reinforce each another.
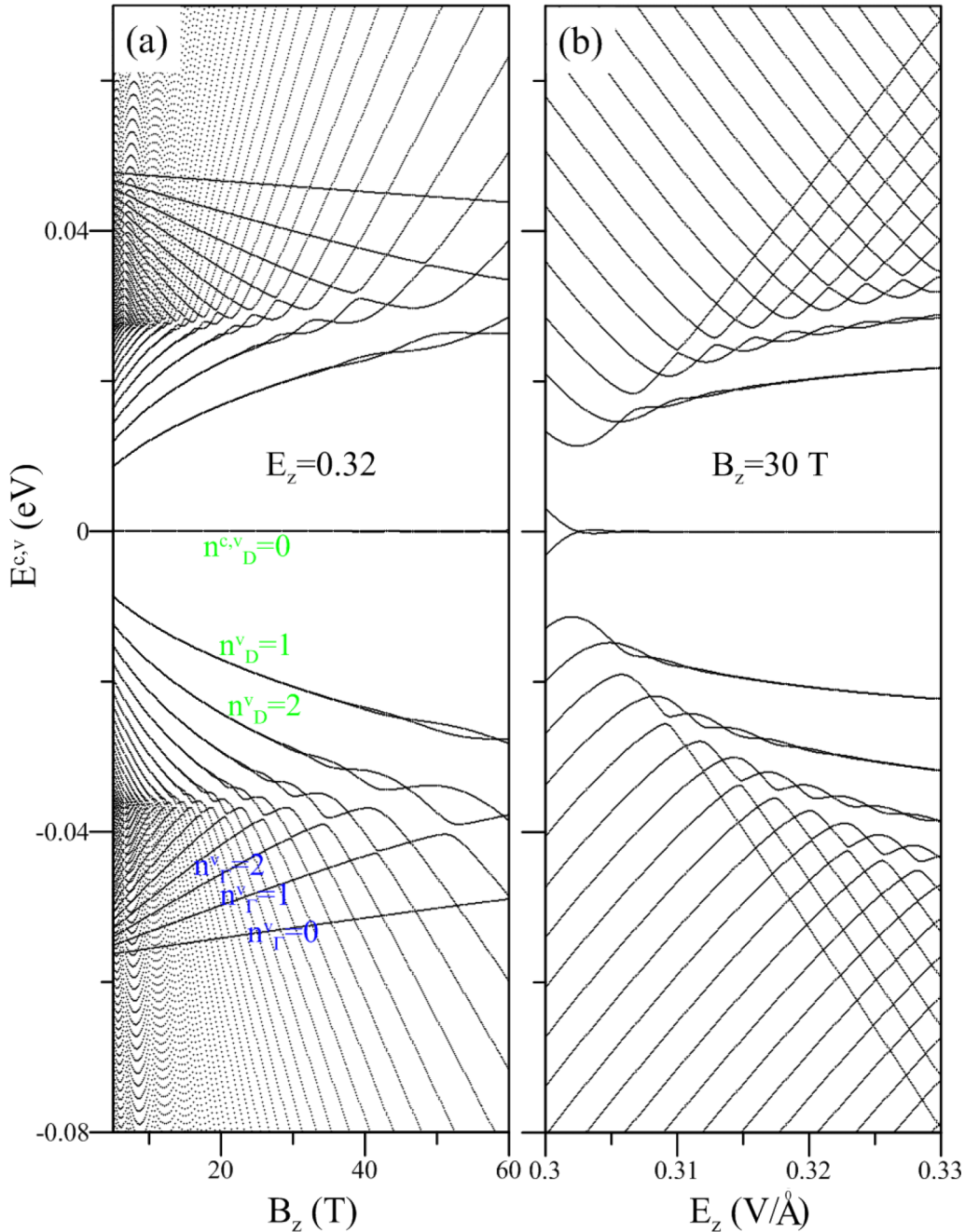
FIG. 5. (a) B_z- and (b) E_z-dependent LL energy spectra.

The main features of the energy bands and LL spectra are directly reflected in the DOS, which is defined as $D(\omega) = \sum_{n^c,n^v} \int_{1^{st}BZ} \delta(\omega - E^{c,v}(n,k))dk$. In the absence of any fields or in the presence of weak E_z fields, the band-edge states of parabolic bands create gap-dependent shoulder-like structures, e.g., $E_z = 0.29$ in Fig. 7(a) shown as the blue curve. The initial structures are replaced by a valley-like structure due to the deformed Dirac cone displayed in Fig. 2(g), when the gap transition happens at $E_z = E_c$ [Fig. 7(b)]. The symmetric peaks in the logarithmically divergent form, corresponding to the saddle points in energy bands, come to exist on both sides of this valley. The special structures are more obvious when $E_z > E_c$, especially for the extended valley structure in

Figs. 7(c) and 7(d). Furthermore, shoulder structures arise from the extremum Γ points. The prominent peaks and shoulders gradually move away from the Fermi energy with a further increase in E_z. The E_z-induced drastic changes in the energy bands could be verified from STS measurements of the energy gap and the valley-like, shoulder, and peak structures [41,42].

A uniform magnetic field induces several δ-function-like peaks. The height and spacing of peaks reflect eigenstate degeneracy and energy dispersion of $B_z = 0$. At $E_z < E_c$, the low-frequency DOS peaks have uniform height with four-fold degeneracy and almost the same spacing as shown as the red curve in Fig. 7(a), mainly due to the quantization for a parabolic band [see Fig. 2(e)]. But for $E_z \gtrsim E_{z,c}$, the unusual
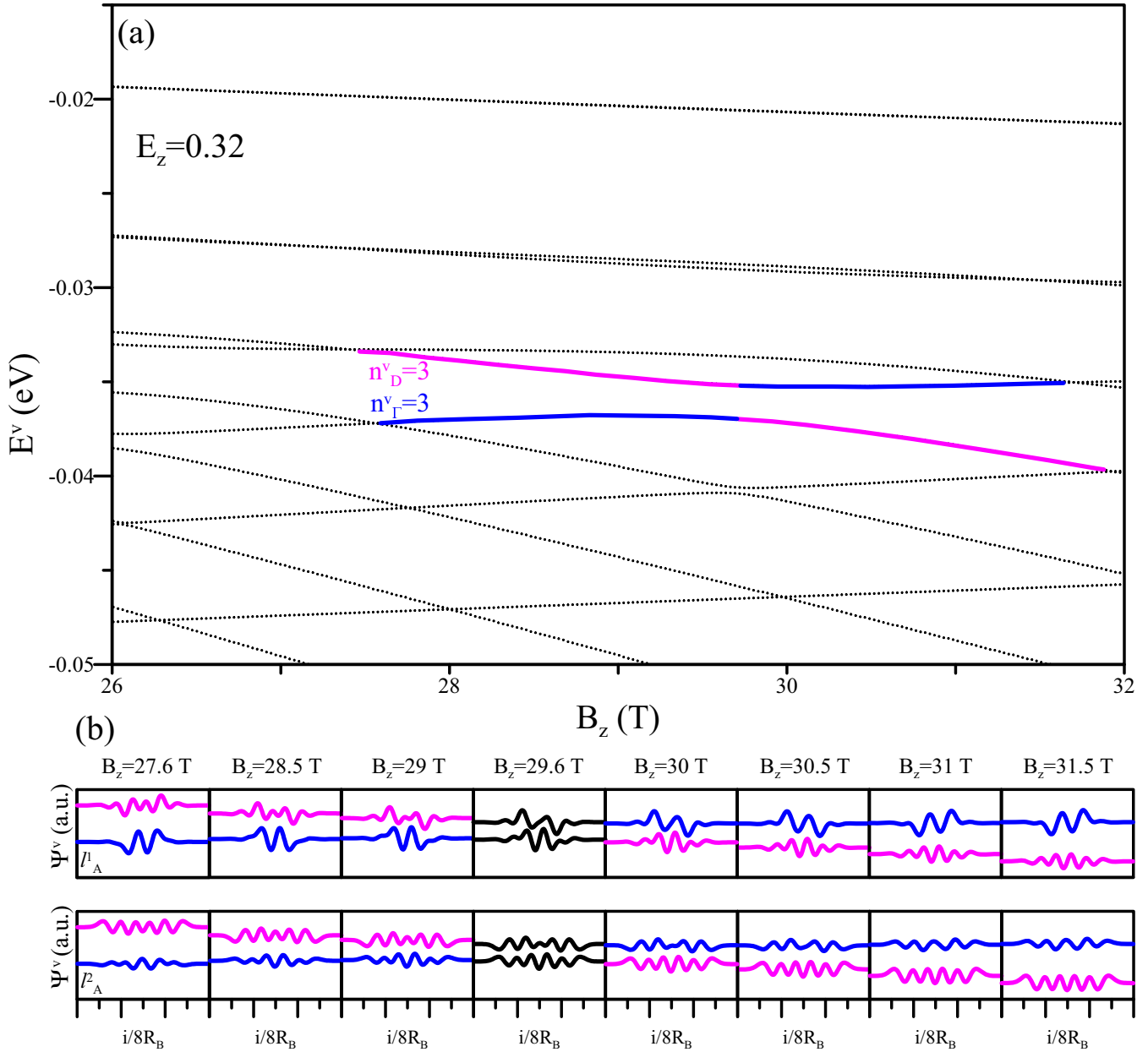
FIG. 6. (a) LL anticrossing energy spectrum (blue and pink curves), and (b) dramatic transformation between oscillation modes on the first and second layers.

features appear for the energy ranges in Figs. 7(b)–7(d). There is a pair of peaks centered around the Fermi level at $E_z = E_{z,c}$ in Fig. 7(b). With an increase in E_z, a very prominent peak, with eightfold degeneracy, appears at $E_F = 0$ as we show in Fig. 7(c). Similar peaks, which come from the quantized Dirac cone, could survive at stronger electric fields as apparent in Fig. 7(d). The double-peak character at higher energies is due to two anticrossing LLs. Apparently, all the low-lying peaks present highly nonuniform spacings. The STS measurements on the main features of low-energy LL peaks could provide useful information about the diverse magnetic quantizations.

Monolayer and bilayer phosphorus are in sharp contrast with graphene with respect to their electronic properties such

as the field-dependent band structures and LLs. The Dirac cone for graphene can yield a square-root dependence on B_z for the LL energy spectrum. Each LL is eightfold degenerate because of the hexagonal symmetry (or two equivalent valleys) [39]. The AA- and AB-stacked bilayer graphene structures are semimetals with band overlaps. The AA stacking could be regarded as a superposition of two monolayers of graphene in magnetic quantization; that is, this system has the usual energy spectra and LL wave functions. However, an electric field applied to AB stacking leads to an energy gap and valley-split LLs. The LL degeneracy is reduced by half by destroying the mirror symmetry about the $z = 0$ plane. Furthermore, each split LL subgroup exhibits anticrossing behavior. However, the coexistent magnetic quantization, which originates from the
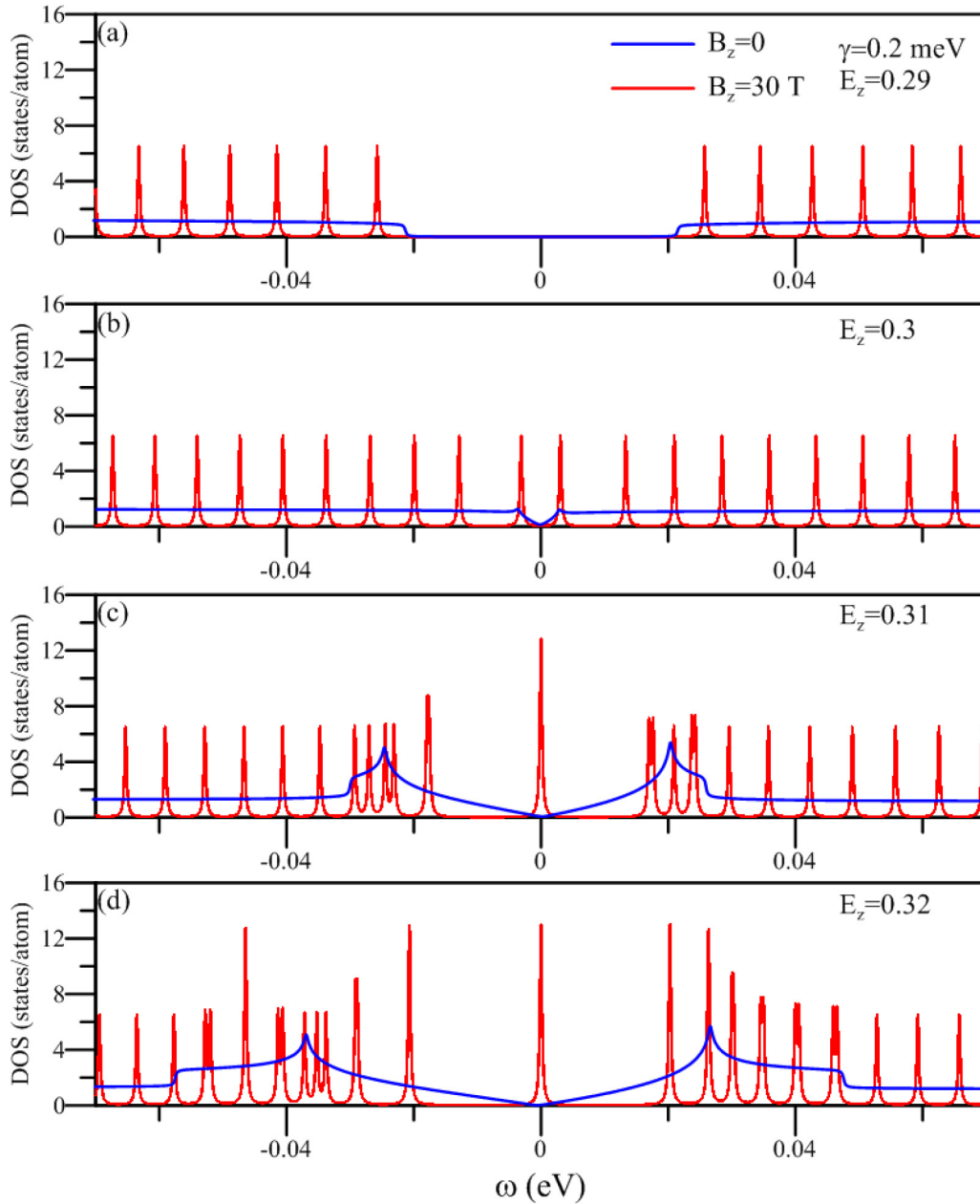
FIG. 7. DOSs of bilayer phosphorus at $B_z = 0$ and 30 T (blue and red curves) (a)–(d) under various E_z. $\gamma = 0.2$ meV is the broadening factor in calculating DOS.

Dirac-cone structure and the two-constant loops in one valence (conduction) energy band, is absent in graphene systems. The lattice symmetries and the intralayer and interlayer atomic interactions are responsible for the crucial differences.

IV. CONCLUDING REMARKS

The generalized tight-binding model is developed to investigate the electronic properties of monolayer and bilayer phosphorus in perpendicular uniform electric and magnetic fields. The feature-rich characteristics include the E_z-induced drastic changes in the energy band structures and the B_z-created diverse magnetic quantizations. The spatial distributions of the subenvelope functions are crucial in illustrating the main features of the LLs, some of which, such as the quantum number and subgroup classification, can be determined by the number of zero points and the dominant sublattices. This method provides an approach for describing other main-stream 2D materials under various external fields. For example, important differences exist between phosphorene and group-IV systems in quantization phenomena [36]. Furthermore, it could be employed in single- and many-particle theories to explore the essential physical properties, such as the magneto-optical and Coulomb excitations [43,44].

Single-layer phosphorene only exhibits a monotonic dependence on E_z and B_z in its energy spectra and wave functions. The electric and magnetic fields can create diverse phenomena in a bilayer system, such as the gap transition, coexistent linear, oscillatory and parabolic bands, two subgroups of LLs, uniform and nonuniform LL energy spacings, and

frequent crossings and anticrossings. The subenvelope functions present dramatic changes between the well-behaved and multioscillation modes during the hybridization of two mixed LLs. The former is identical with a quantized simple harmonic oscillator, while the latter means a perturbed distribution mode. The main characteristics for the energy bands and LLs are reflected in the DOS as various structures, including valleys, shoulders, and logarithmic and δ-function-like peaks. The number, form, height, and energy of the LL peaks near the Fermi level are closely related to the magnetic quantization arising from the Dirac cone and the two constant-energy loops,

e.g., a stronger peak at $E = 0$ and the double-peak structures. The STS measurements on the low-lying special structures would be useful tools in understanding the competitive or cooperative relations among the external fields, and the intralayer and interlayer atomic interactions.

[1] M. Xu, T. Liang, M. Shi, and H. Chen, Chem. Rev. **113**, 3766 (2013).

[2] S. Z. Butler, S. M. Hollen, L. Cao, Y. Cui, J. A. Gupta, H. R. Gutiérrez, T. F. Heinz, S. S. Hong, J. Huang, A. F. Ismach, E. Johnston-Halperin, M. Kuno, V. V. Plashnitsa, R. D. Robinson, R. S. Ruoff, S. Salahuddin, J. Shan, L. Shi, M. G. Spencer, M. Terrones, W. Windl, and J. E. Goldberger, ACS Nano **7**, 2898 (2013).

[3] F. Wang, Z. Wang, Q. Wang, F. Wang, L. Yin, K. Xu, Y. Huang, and J. He, Nanotech. **26**, 292001 (2015).

[4] B. Aissa, N. K. Memon, A. Ali, and M. K. Khraisheh, Front. Mater. **2**, 58 (2015).

[5] N. Takagi, C. L. Lin, K. Kawahara, E. Minamitani, N. Tsukahara, M. Kawai, and R. Arafune, Prog. Surf. Sci. **90**, 1 (2015).

[6] M. Derivaz, D. Dentel, R. Stephan, M. Hanf, A. Mehdaoui, P. Sonnet, and C. Pirri, Nano Lett. **15**, 2510 (2015).

[7] F. F. Zhu, W. J. Chen, Y. Xu, C. L. Gao, D. D. Guan, C. H. Liu, D. Qian, S. C. Zhang, and J. F. Jia, Nat. Mater. **14**, 1020 (2015).

[8] Q. H. Wang, K. Kalantar-Zadeh, A. Kis, J. N. Coleman, and M. S. Strano, Nat. Nanotech. **7**, 699 (2012).

[9] L. Li, Y. Yu, G. J. Ye, Q. Ge, X. Ou, H. Wu, D. Feng, X. H. Chen, and Y. Zhang, Nat. Nanotechnol. **9**, 372 (2014).

[10] H. Liu, A. T. Neal, Z. Zhu, Z. Luo, X. Xu, D. Tománek, and P. D. Ye, ACS Nano **8**, 4033 (2014).

[11] J. R. Brent, N. Savjani, E. A. Lewis, S. J. Haigh, D. J. Lewis, and P. O'Brien, Chem. Commun. **50**, 13338 (2014).

[12] P. Yasaei, B. Kumar, T. Foroozan, C. Wang, M. Asadi, D. Tuschel, J. E. Indacochea, R. F. Klie, and A. Salehi-Khojin, Adv. Mater. **27**, 1887 (2015).

[13] J. Kang, J. D. Wood, S. A. Wells, J.-H. Lee, X. Liu, K. S. Chen, and M. C. Hersam, ACS Nano **9**, 3596 (2015).

[14] S. Lange, P. Schmidt, and T. Nilges, Inorg. Chem. **46**, 4028 (2007).

[15] T. Nilges, M. Kersting, and T. Pfeifer, J. Solid State Chem. **181**, 1707 (2008).

[16] M. Kopf, N. Eckstein, D. Pfister, C. Grotz, I. Kruger, M. Greiwe, T. Hansen, H. Kohlmann, and T. Nilges, J. Cryst. Growth **405**, 6 (2014).

[17] Y. Takao and A. Morita, Phys. B (Amsterdam) **105**, 93 (1981).

[18] A. N. Rudenko and M. I. Katsnelson, Phys. Rev. B **89**, 201408 (2014).

[19] J. Dai and X. C. Zeng, J. Phys. Chem. Lett. **5**, 1289 (2014).

[20] S. Zhang, J. Yang, R. Xu, F. Wang, W. Li, M. Ghufran, Y. W. Zhang, Z. Yu, G. Zhang, Q. Qin, and Y. Lu, ACS Nano **8**, 9590 (2014).

[21] C. Q. Han, M. Y. Yao, X. X. Bai, L. Miao, F. Zhu, D. D. Guan, S. Wang, C. L. Gao, C. Liu, D. Qian, Y. Liu, and J. F. Jia, Phys. Rev. B **90**, 085101 (2014)

[22] S. Balendhran, S. Walia, H. Nili, S. Sriram, and M. Bhaskaran, Small **11**, 640 (2015).

[23] X. Y. Zhou, R. Zhang, J. P. Sun, Y. L. Zou, D. Zhang, W. K. Lou, F. Cheng, G. H. Zhou, F. Zhai, and K. Chang, Sci. Rep. **5**, 12295 (2015).

[24] J. M. Pereira, Jr., and M. I. Katsnelson, Phys. Rev. B **92**, 075437 (2015).

[25] S. Yuan, E. van Veen, M. I. Katsnelson, and R. Roldán, Phys. Rev. B **93**, 245433 (2016).

[26] L. Li, F. Yang, G. J. Ye, Z. Zhang, Z. Zhu, W. Lou, X. Zhou, L. Li, K. Watanabe, T. Taniguchi, K. Chang, Y. Wang, X. H. Chen, and Y. Zhang, Nat. Nanotech. **11**, 593 (2016).

[27] J. L. Lado and J. Fernández-Rossier, 2D Mater. **3**, 035023 (2016).

[28] Z. T. Jiang, Z. T. Lv, and X. D. Zhang, Phys. Rev. B **94**, 115118 (2016).

[29] H. C. Chung, C. P. Chang, C. Y. Lin, and M. F. Lin, Phys. Chem. Chem. Phys. **18**, 7573 (2016).

[30] T. Low, A. S. Rodin, A. Carvalho, Y. Jiang, H. Wang, F. Xia, and A. H. Castro Neto, Phys. Rev. B **90**, 075434 (2014).

[31] X. Ling, H. Wang, S. Huang, F. Xia, and M. S. Dresselhaus, Proc. Natl. Acad. Sci. USA **112**, 4523 (2015).

[32] C. Dutreix, E. A. Stepanov, and M. I. Katsnelson, Phys. Rev. B **93**, 241404(R) (2016).

[33] K. Dolui and S. Y. Quek, Sci. Rep. **5**, 11699 (2015).

[34] Q. Liu, X. Zhang, L. B. Abdalla, A. Fazzio, and A. Zunger, Nano Lett. **15**, 1222 (2015).

[35] C. Y. Lin, J. Y. Wu, Y. J. Ou, Y. H. Chiu, and M. F. Lin, Phys. Chem. Chem. Phys. **17**, 26008 (2015).

[36] S. C. Chen, C. L. Wu, J. Y. Wu, and M. F. Lin, Phys. Rev. B **94**, 045410 (2016).

[37] C. L. Lu, C. P. Chang, Y. C. Huang, R. B. Chen, and M. L. Lin, Phys. Rev. B **73**, 144427 (2006).

[38] J. H. Ho, Y. H. Lai, Y. H. Chiu, and M. F. Lin, Phys. E (Amsterdam) **40**, 1722 (2008).

[39] Y. H. Lai, J. H. Ho, C. P. Chang, and M. F. Lin, Phys. Rev. B **77**, 085426 (2008).

[40] Y. H. Ho, C. W. Chiu, W. P. Su, and M. F. Lin, Appl. Phys. Lett. **105**, 222411 (2014).

[41] Y. J. Song, A. F. Otte, Y. Kuk, Y. Hu, D. B. Torrance, P. N. First, W. A. de Heer, H. Min, S. Adam, M. D. Stiles, A. H. MacDonald, and J. A. Stroscio, Nature **467**, 185 (2010).

[42] S. Jung, G. M. Rutter, N. N. Klimov, D. B. Newell, I. Calizo, A. R. Hight-Walker, N. B. Zhitenev, and J. A. Stroscio, Nat. Phys. **7**, 245 (2011).

[43] Y. H. Ho, Y. H. Chiu, D. H. Lin, C. P. Chang, and M. F. Lin, ACS Nano **4**, 1465 (2010).

[44] J. Y. Wu, S. C. Chen, O. Roslyak, G. Gumbs, and M. F. Lin, ACS Nano **5**, 1026 (2011).